Identifying Isotropic Events Using a Regional Moment Tensor Inversion

S. R. Ford, D. S. Dreger, W. R. Walter

Disclaimer

This document was prepared as an account of work sponsored by an agency of the United States government. Neither the United States government nor Lawrence Livermore National Security, LLC, nor any of their employees makes any warranty, expressed or implied, or assumes any legal liability or responsibility for the accuracy, completeness, or usefulness of any information, apparatus, product, or process disclosed, or represents that its use would not infringe privately owned rights. Reference herein to any specific commercial product, process, or service by trade name, trademark, manufacturer, or otherwise does not necessarily constitute or imply its endorsement, recommendation, or favoring by the United States government or Lawrence Livermore National Security, LLC. The views and opinions of authors expressed herein do not necessarily state or reflect those of the United States government or Lawrence Livermore National Security, LLC, and shall not be used for advertising or product endorsement purposes.

1 # Identifying isotropic events using a regional moment tensor inversion
2

3 Sean R. Ford [a,b], Douglas S. Dreger [a], William R. Walter [b]
4
5 [a] Berkeley Seismological Laboratory, Berkeley, California-94720, USA
6 [b] Lawrence Livermore National Laboratory, Livermore, California-94550, USA

7
8
9 Abstract
10

11 We calculate the deviatoric and isotropic source components for 17 explosions at the Nevada
12 Test Site, as well as 12 earthquakes and 3 collapses in the surrounding region of the western US,
13 using a regional time-domain full waveform inversion for the complete moment tensor. The
14 events separate into specific populations according to their deviation from a pure double-couple
15 and ratio of isotropic to deviatoric energy. The separation allows for anomalous event
16 identification and discrimination between explosions, earthquakes, and collapses. Confidence
17 regions of the model parameters are estimated from the data misfit by assuming normally
18 distributed parameter values. We investigate the sensitivity of the resolved parameters of an
19 explosion to imperfect Earth models, inaccurate event depths, and data with a low signal-to-noise
20 ratio (SNR) assuming a reasonable azimuthal distribution of stations. In the band of interest
21 (0.02-0.10 Hz) the source-type calculated from complete moment tensor inversion is insensitive
22 to velocity models perturbations that cause less than a half-cycle shift (<5 sec) in arrival time
23 error if shifting of the waveforms is allowed. The explosion source-type is insensitive to an
24 incorrect depth assumption (for a true depth of 1 km), and the goodness-of-fit of the inversion
25 result cannot be used to resolve the true depth of the explosion. Noise degrades the explosive
26 character of the result, and a good fit and accurate result are obtained when the signal-to-noise
27 ratio (SNR) is greater than 5. We assess the depth and frequency dependence upon the resolved
28 explosive moment. As the depth decreases from 1 km to 200 m, the isotropic moment is no
29 longer accurately resolved and is in error between 50-200%. However, even at the most shallow
30 depth the resultant moment tensor is dominated by the explosive component when the data has a
31 good SNR.

32

32   1. Introduction
33
34   The full seismic moment tensor (2nd rank tensor, M_{ij}) is a general representation of any seismic
35   point source in terms of force-couples (Gilbert, 1971), and is used in tectonic studies to describe
36   the double-couple (DC) nature of shear-faulting. However, M_{ij} is sufficiently general to represent
37   non-DC seismic sources (for an outstanding review of non-DC earthquakes, see Julian et al.,
38   1998). The isotropic component of the moment tensor ($M_{ij}^{ISO} = \delta_{ij} (M_{11}+M_{22}+M_{33})/3$) is related to
39   the volume change associated with a source (Muller, 1973), and is significant in the case of an
40   explosion. The deviatoric component of M_{ij} ($M_{ij}^{DEV} = M_{ij} \Box \delta_{ij} (M_{11}+M_{22}+M_{33})/3$) is most often
41   employed to define the DC source, but can also describe the volume-compensated linear vector
42   dipole (CLVD), which has been used to explain deep seismicity (e.g., Knopoff and Randall,
43   1970; Kawakatsu, 1990), and has also been shown to result from complex faulting events (Kuge
44   and Lay, 1994). Complex sources like a tensile crack require a combination of deviatoric and
45   isotropic components, and the opening-crack has been suggested as a source for some volcanic
46   events (e.g., Foulger et al., 2004; Templeton and Dreger, 2006) and the closing-crack for mine
47   collapses (e.g. Pechmann et al., 1995; Bowers and Walter, 2002).
48
49   The inversion of seismic data to calculate the deviatoric moment tensor has been done for over
50   30 years in both the time-domain (e.g., Stump and Johnson, 1977) and frequency domain (e.g.,
51   Gilbert and Dziewonski, 1975). The inversion of full-waveform data from regional events is now
52   routine practice at several institutions including the Berkeley Seismological Laboratory since
53   1993 (Romanowicz et al., 1993), where the results are housed at the Northern California
54   Earthquake Data Center (NCEDC; www.ncedc.org/ncedc/mt.html). Recently, Minson and
55   Dreger (2008) have extended the full-waveform inversion to calculate all six independent
56   elements of the symmetric moment tensor, which allows for estimation of the isotropic
57   component of the source.
58
59   The concept of using intermediate period waveforms, particularly surface wave radiation
60   patterns, to identify explosions goes back more than 40 years. Early results were disappointing
61   due to the presence of unexpected Love waves and occasional reversed Rayleigh waves from
62   tectonic release (e.g. Press and Archambeau, 1962; Brune and Pommery, 1963). However
63   despite these complexities, the well-established ratio of surface wave magnitude (M_S) to body
64   wave magnitude (m_b) separates earthquakes from explosions even when there is significant
65   tectonic release, indicating there are differences in the waveforms, even if the explosion signals
66   do not always conform to the simple isotropic model. Identification of events with demonstrably
67   significant isotropic components can aid in yield determination (e.g., Stevens and Murphy, 2001;
68   Patton, 1991) and possibly nuclear test discrimination (e.g., Woods et al., 1993). Given and
69   Mellman (1986) inverted teleseismic long-period fundamental mode surface waves from 18 large
70   ($m_b \geq 5.5$) nuclear test explosions at the Nevada Test Site (NTS) to calculate a three-parameter
71   source model. The model was used to estimate the isotropic moment (M_I), along with the strike
72   and moment of an assumed vertical strike-slip component, and they found no improvement in
73   yield estimation when using M_I as opposed to M_S. Patton (1988) added higher mode Rayleigh
74   wave data from stations at regional distances and performed an inversion for the full moment
75   tensor with an additional directed force component to represent spall for the HARZER explosion
76   ($m_b 5.6$) at NTS. The study was later extended to 16 nearby explosions and the relationship
77   between total seismic moment (M_0) and yield agreed well with previous results using M_S (Patton,

78   1991). Dreger and Woods (2002) examined three NTS nuclear tests using data from three

79   TERRAscope stations in southern California (180° < azimuth < 230°). The work presented here

80   amends and extends their study to 14 more nuclear tests at the NTS, three collapses (two mine

81   collapses and one explosion cavity collapse), and 12 earthquakes near the NTS (Figure 1; Table

82   1).

83

84   2. Data and Method

85

86   We implement the time-domain full-waveform inversion of regional data for the complete

87   moment tensor devised by Minson and Dreger (2008) after Herrmann and Hutcheson (1993)

88   based on the work of Langston (1981). In general, synthetic seismograms are represented as the

89   linear combination of fundamental Green's functions where the weights on these Green's

90   functions are the individual moment tensor elements. The Green's functions for a one-

91   dimensional (1-D) velocity model of eastern California and western Nevada (Table 2; Song et

92   al., 1996) are calculated as synthetic displacement seismograms using a frequency-wavenumber

93   integration method (Saikia, 1994). The synthetic data is filtered with a 4-pole acausal

94   Butterworth filter with a low-corner of 0.02 Hz and a high-corner of 0.05 Hz and 0.1 Hz for

95   events with $M_W \geq 4$ and $M_W < 4$, respectively. At these frequencies, where dominant

96   wavelengths are tens of kilometers, we assume a point source for the low-magnitude regional

97   events investigated in this study. The point source assumption allows for linearization in the

98   time-domain, which is where we carry out the least-squares inversion.

99

100   We analyzed events that were digitally recorded with a high signal-to-noise ratio by more than

101   two regional broadband stations. Three-component data was collected from a total of 52 stations

102   from the US National Seismic Network, IRIS/USGS, Berkeley Digital Seismic Network, Trinet,

103   and the Lawrence Livermore National Laboratory (LLNL) network (Figure 1; Supplemental

104   Table 1). All data is freely available from IRIS via the internet except the LLNL historic network

105   data, which is available on compact disk (Walter et al., 2004). Not all stations recorded all

106   events, and a total of 16 stations were used in the inversion of the explosion data, which are

107   listed in Figure 1. We remove the instrument response, rotate to the great-circle frame, integrate

108   to obtain displacement, and use the same filter as for the synthetic seismograms. The LLNL

109   network (white triangles in Figure 1) was composed of Sprengnether instruments with limited

110   long-period response, and for those data we used a passband of 10 - 30 seconds for both the data

111   and synthetics.

112

113   We calibrated the algorithm by calculating the full moment tensor for the 1992 Little Skull

114   Mountain event (Figure 1). We find a solution at all depths within 5 km of the reported depth.

115   The depth that produces Green's functions that best fit the data is used in the final solution. Fit is

116   quantified by the variance reduction (VR), which is a normalized variance given by

117

$$\text{VR} = \left[1 - \frac{\sum_i (d_i - s_i)^2}{\sum_i d_i^2} \right] \times 100 , \tag{1}$$

118

119 where *i* are the displacements at all times for all components at all stations, and *d,* and *s* are the
120 data and synthetic respectively..
121
122 We also allow the Green's functions calculated at a given distance to shift relative to the data to
123 address small hypocentral errors and uncertainty in the velocity model used to compute the
124 Green's functions. The shift that produces the best fit is used in the final solution. We limit the
125 shift to less than 5 and 3 sec for high-pass corners of 0.05 and 0.10 Hz, respectively. The allowed
126 time shift is large enough to make up for small hypocentral errors, but small enough to disallow
127 cycle-skipping that could produce erroneous mechanisms. The sensitivity of the time shift
128 relative to the assumed velocity model will be discussed later in the paper. The full moment
129 tensor solution is decomposed to an isotropic and deviatoric component in Figure 2a. We
130 calculate the total scalar moment (M_0) as defined by Bowers and Hudson (1999), where M_0 is
131 equal to the sum of the isotropic moment ($M_{\text{ISO}} = (M_{11}+M_{22}+M_{33})/3$) and deviatoric moment
132 (M_{DEV}), which is the largest deviatoric eigenvalue. For the Little Skull Mountain event we find
133 $M_0 = 3.7 \times 10^{17}$ N-m ($M_{\text{W}} = 5.6$), and the solution has a negligible isotropic moment ($M_{\text{ISO}} =$
134 -0.31×10^{17} N-m) so there is little change between the full and deviatoric solutions. The solution
135 fits the data very well (Figure 2b) and is similar to the double-couple solution of Walter (1993),
136 the deviatoric solution of Ichinose et al. (2003), and the full solution of Dreger and Woods
137 (2002).
138
139 With the same algorithm we calculate the full moment tensors of 17 nuclear test explosions at the
140 NTS (Figure 1). In the case of explosions and collapses we calculate Green's functions at a depth
141 of 1 km. The sensitivity of this assumption will be investigated later in the paper. An example of
142 the analysis is given by the solution for the 1991 HOYA test in Figure 3, where both the full and
143 deviatoric moment tensors are given. The largest component in the decomposition is isotropic
144 and it contributes 70% of the total scalar moment.
145
146 3. Results
147
148 It is difficult to grasp the source-type from the standard focal mechanism plot for events with a
149 large non-DC component. For example, one cannot discern the relative contributions of the
150 isotropic and deviatoric components from the full focal mechanism in Figure 3 for the HOYA
151 explosion. In order to get at the tectonic contribution to the explosion, one could separate the
152 deviatoric component into a DC and a CLVD that share the orientation of the major axis, but
153 decompositions of this type are non-unique, where for example the DC and CLVD
154 decomposition could be replaced by two DCs (see Julian et al. (1998) for further
155 decompositions). In an attempt to better characterize mechanisms we follow the source-type
156 analysis described in Hudson et al. (1989) and calculate -2ε and *k,* which are given by
157

$$\square = \frac{-m\square}{|m\square|},$$ (2)

158
159 and
160

$$k = \frac{M_{\text{ISO}}}{|M_{\text{ISO}}| + |m'_3|},\qquad\qquad(3)$$

161

162   where m'_1, m'_2 and m'_3 are the deviatoric principal moments for the N, P, and T axes,
163   respectively, and $|m'_1| \leq |m'_2| \leq |m'_3|$. ε is a measure of the departure of the deviatoric component
164   from a pure DC mechanism, and is 0 for a pure double-couple and ±0.5 for a pure CLVD. k is a
165   measure of the volume change, where +1 would be a full explosion and −1 a full implosion. -2ε
166   and k for the Little Skull Mountain earthquake and NTS explosion, HOYA, are given in Figure
167   4a. The earthquake is almost at the origin, which defines a pure DC, whereas the nuclear test is
168   near where a theoretical explosion would plot. In order to estimate formal error in the fit, we
169   create moment tensor populations by bootstrapping the residuals of the fit $n$times with
170   replacement and then use those populations of size n to calculate -2ε and k, resulting in their
171   own populations to which we fit normal distributions. Figure 4a shows the population of $n =$
172   1000 along with the 95% confidence region for the DIVIDER explosion. Increasing n resulted in
173   no change to the confidence regions.

174

175   Hudson et al. (1989) transform the parameters -2ε and k so that the displayed plot will have
176   equal normal probability areas based on the assumption that the smallest principal moments can
177   take any value between ± the largest absolute principal moment (Julian et al., 1998). The plot
178   derived this way is the source-type plot and it is shown in Figure 4b for the parameters from the
179   Little Skull Mt. earthquake and HOYA explosion. Figure 4b also shows the transformed
180   bootstrap population for the DIVIDER explosion and its associated 95% confidence region. The
181   transformation makes the assumption of normality in the error distribution valid as can be seen
182   by the improved fit of an error ellipse to the bootstrap population between Figure 4a and b. The
183   Hudson et al. (1989) plot is a superior way to display source-type and analyze error in the
184   parameters. The error ellipses are not shown for the Little Skull Mt. earthquake or HOYA
185   explosion examples because the error regions are too small to notice a difference due to the
186   transformation.

187

188   We carry out similar analyses for 11 more earthquakes and three collapses (one cavity and two
189   mine) and produce the source-type plot in Figure 5 along with the 95% confidence regions. The
190   nuclear tests occupy the region where $k > 0.5$, the earthquakes cluster near the origin, and the
191   collapses plot almost exactly at (1,-5/9), which is the location for a closing crack in a Poisson
192   solid. Deviations from these trends will be discussed later. Moment tensor elements and source-
193   type parameters for all events are given in Table 3.

194

195   4. Sensitivity Analysis

196

197   The relatively small area of the confidence regions given in Figure 5 and the excellent synthetic
198   seismogram fit to the data as quantified by VR gives us great confidence that the assumed
199   velocity model and depth are correct and the estimated moment tensor solutions are robust.
200   However, these measures of goodness-of-fit assume the underlying model used to invert the data
201   is correct. In the following section we will test these assumptions with synthetic data from a
202   theoretical explosion ($-2\varepsilon=0$, $k=1$) created for two experimental geometries. The first geometry,
203   referred to as 'Ideal', is eight stations at distance increments between 100 and 300 km each

204 separated by 45° in azimuth. The second station geometry mirrors the analysis for the HOYA
205 explosion. The station distributions are given in Figure 6. The synthetic data are filtered in the
206 same two bands (20-50s and 10-50s) used in the analysis and when combined with the two
207 geometries results in 4 scenarios.

209 4.1. Noise

211 The error analysis presented above is due to misfit of the data by the least-squares inversion. Part
212 of the misfit may be due to nonstationary noise and we test the sensitivity of the inversion to
213 different signal-to-noise ratios (SNR). In order to best approximate real-world noise conditions,
214 we derive the noise signal from data prior to the first arrival from the nuclear test METROPOLIS
215 (10 Mar 90) at station ANMO for all three components. The amplitude of this noise signal is
216 bandpassed to match the synthetic data and multiplied by a factor so as to create a final synthetic
217 signal with the desired SNR (ratio of synthetic data root-mean-square amplitude to noise root-
218 mean-square amplitude).

220 The noise analysis has very little frequency dependence so for clarity we only show results from
221 the analysis in the 20 - 50 sec frequency band in Figure 7a. The Ideal configuration produces the
222 best scenario where a large k is retrieved (>0.3) when the SNR is greater than 2. For all scenarios
223 $k > 0.5$ when SNR > 5. Typically, we use data with an SNR greater than 10, however there are a
224 few cases where the SNR is close to 3. An example of this type of data is given in Figure 8 for
225 the DIVIDER explosion, which produced signal that was right on the limit of acceptable SNR
226 (see stations ELK and MHC) but still produced a well-fit solution.

228 4.2. Incorrect Depth

230 Another source of error not incorporated into the formal error analysis is incorrectly calculated
231 Green's functions due to ignorance of the true event depth. The method that produces the results
232 presented above attempts to find an optimal depth for the earthquakes by perturbing the reported
233 depth a few kilometers, performing the inversion, and finding the best-fit solution. For all
234 explosions and collapses the depth is fixed at 1 km. If this method were to be used for an event
235 with an unknown source type, the depth could be an important source of error, as well as an
236 important parameter for identification. We perform another synthetic test in which an explosion
237 at 1 km is inverted with Green's functions calculated at varying depths.

239 The source depth analysis is not greatly affected by the two station configurations considered
240 here, therefore we only show results for the HOYA configuration in Figure 7b. The result at an
241 incorrect depth of 2 km is virtually indistinguishable from the true answer. When the source is
242 moved to 3 km depth there is a small step decrease in k due to a layer in the velocity model that
243 begins at 2.5 km depth. However, $k > 0.5$ for incorrect depths < 17 km with slightly more
244 sensitivity in k and worse fit in the high frequency band (10 - 50 sec) compared to the low
245 frequency band (20 - 50 sec). The relative insensitivity of the solution to mislocated depth for an
246 explosion is different than is observed for DC events. Dreger and Woods (2002) show that the
247 VR of the Little Skull Mountain earthquake solution is definitively maximized at the assumed
248 true event depth. Thus while the depth sensitivity of explosions is poor, the method is able to

249 determine depth of non-explosion sources, which also provides an important level of event
250 screening.
251
252 4.3. Velocity Model
253
254 Finally, we test how error in the assumed Earth structure is mapped through the Green's
255 functions to error in the solution. We start with the well-calibrated Song et al. (1996) velocity
256 model (Table 2) and perturb the velocities and depths of the layers using averaged parameters
257 from another plausible velocity model (WestUS; Ammon, 1999) and a model from Southern
258 California (SoCal; Dreger and Helmberger, 1990). Perturbed values are given in Table 4, which
259 result in a population of 243 models.
260
261 In order to produce a sensitivity test that best mimics our analysis, we use the time shift rule to
262 filter the models. This means that we only allow velocity models that produce Green's functions
263 where the time shift between data and synthetics that produces the best-fit solution is less than or
264 equal to 5 or 3 sec from the theoretical arrival time for high-pass corners of 0.05 or 0.10 Hz,
265 respectively. Primarily due to the velocity model filtering there is little difference among the
266 scenarios so we only show source-type plots for the HOYA configuration in the 20 - 50 sec
267 frequency band in Figure 7c. For this scenario the number of acceptable models is reduced to 88,
268 and although not all possible combinations of model parameters are used, each parameter
269 perturbation given in Table 4 is employed at least once.
270
271 Without shifting there are a few velocity models that produce well-fit solutions (VR>90%) with
272 mechanisms that are almost purely DC. However, when shifting is allowed all velocity models
273 produce good fits with highly explosive sources ($k\sim>0.4$).
274
275 4.4. Free-surface effects
276
277 Another consideration is the ability to resolve displacements for explosions near the surface.
278 Since tractions normal to the vertical vanish at the free surface, the excitation coefficients
279 associated with those tractions must vanish (Julian et al., 1998). Therefore at the free surface the
280 moments of M_{13}, M_{23}, and the isotropic part of the M_{ij} cannot be resolved. Given and Mellman
281 (1986) showed that at a source depth of 1 km the fundamental mode excitation functions
282 associated with the moments listed previously effectively go to zero. We investigate the potential
283 problems associated with vanishing traction at the free surface by inverting noisy data from a
284 synthetic explosion source at depths between 200 and 1000 m in a three-layer 1D velocity model
285 using Green's functions calculated at those same depths.
286
287 The ability to resolve an explosive component is dependent on the station distribution, frequency
288 and SNR of the analysis, therefore Figure 9 shows all 4 scenarios. An explosive component
289 ($k>0.5$) can be resolved under favorable noise conditions at a depth greater than 300 m for all
290 scenarios, though with error in M_{ISO} between 50-150% (Figure 9a-d). The error is inversely
291 proportional to the depth. For all scenarios, but the HOYA configuration at 20-50 sec (Figure
292 9a), favorable noise means SNR $\geq$ 6. The change in M_{ISO} is due to a change in M_{33} relative to the
293 other dipole components (Figure 9i-p), and this produces an erroneous deviatoric component.
294 The moment of deviatoric component can be up to 50% of the theoretical isotropic moment

295 (Figure 9e-h) and since it is related to the error in M_{ISO} it is inversely proportional to the depth.
296 At less than 200 m depth, the synthetic displacements become too small and the solution using
297 these particular Green's functions is unreliable.
298
299 5. Discussion
300
301 The populations of earthquakes, explosions, and collapses separate in the source-type plot. These
302 initial results are very encouraging and suggest a discriminant that employs the source-type plot
303 parameters (-2ε, k). Another advantage of the source-type plot is its display of 2-D error regions.
304 In this way one can test a hypothesis that an event has a non-DC component. For example, the
305 earthquake that is furthest to the top-left in Figure 5 is the Frenchman Flat earthquake. The least-
306 squares error analysis allows one to state that the event is significantly non-DC at the 95%
307 confidence level and it plots near the theoretical opening crack. The Frenchman Flat event was
308 also analyzed by Ichinose et al. (2003) and found to be non-DC as well.
309
310 The source-type analysis can also be utilized to estimate model-based error as well. The error
311 introduced by ignorance of the event location and Earth structure can be calculated with a Monte
312 Carlo approach, where several solutions are computed for a priori distributions of the
313 hypocentral location and Earth model obtained from independent analyses. For example,
314 confidence regions for a given hypocentral location as published by the NEIC can act as the a
315 priori location distribution and the hundreds of 1-D velocity models for a given region produced
316 from a Markov Chain Monte Carlo method as in Pasyanos et al. (2006) can act as the velocity
317 model distribution. Each of the moment tensor solutions could then be plotted producing a
318 scatter density, which would aid in the understanding of how parameterization choice
319 nonlinearly affects the moment tensor solutions, and help map the solution space of best-fit
320 moment tensors.
321
322 We try to give some insight to the depth sensitivity of the method with Figure 7b. In previous
323 analyses of crustal earthquakes, the goodness-of-fit (VR) peaks at the correct depth (Dreger and
324 Woods, 2002). If the same behavior is true of explosions, then the method could act as a
325 discriminant if the best depth is very shallow which is atypical of earthquakes. Of course the
326 alternative is also helpful, if an event solution shows the event to be in the typical range of
327 earthquakes, greater than several km then the estimate provides a level of screening if not
328 discrimination. Figure 7b shows that the use of this method as a precise depth discriminant is not
329 plausible for the frequencies used here, though sensitivity does increase for the higher frequency
330 band.
331
332 These results are a demonstration of the fact that an isotropic radiation pattern has no sensitivity
333 to takeoff angle, which depends on depth. As shown by Dreger and Woods (2002) there is
334 limited resolution of the shallow depth of explosions using regional distance data. Although an
335 explosive radiation pattern alone does not have depth sensitivity, the relative excitation of low
336 frequency body waves (Pnl) and Rayleigh waves does enable the method to discern the relatively
337 shallower depths of explosions compared to earthquakes.
338
339 The velocity model analysis shown in Figure 7c suggests that the maximum shift rule used in the
340 analysis is a good proxy for evaluating the appropriateness of the velocity model. The level of

341 departure of a given velocity model from the true model is station distribution, frequency, and
342 SNR dependent. Therefore, it is a good idea to perform this style of sensitivity test to evaluate
343 the amount of deviation a certain experimental setup will allow, because if the velocity model is
344 poorly calibrated then a good fit to the data can be obtained but the solution may be inaccurate.
345
346 Sileny (2004) investigated the sensitivities of the deviatoric solution and found that velocity
347 perturbations of more than 30% and event depths mislocated by two times the actual depth still
348 return an accurate solution. A further consideration is the assumption of an isotropic Earth
349 structure in the presence of anisotropic data, which may produce a spurious CLVD component
350 (Sileny and Vavrycuk, 2002). Fortunately, the 1-D velocity model seems to be a good
351 approximation in the presence of smoothly varying 3-D heterogeneity (Panning et al., 2001) for
352 the frequency band and regional distances employed here.
353
354 The change in moment due to the loss of traction at the free surface affects yield estimation,
355 though event discrimination is still reliable at high SNR. A result of this change in moment is
356 that the deviatoric moment becomes non-zero and could be significant at very shallow depths
357 (Z<500 m) and low SNR (SNR<6). The moment manifests as a CLVD component, which means
358 that interpretation of non-isotropic energy may be flawed for shallow events even with high SNR
359 data. Though as Figure 9 suggests this effect is station configuration, frequency, and SNR
360 dependent. There is quite a difference in M_{ISO} determined for different frequency bands for the
361 HOYA configuration (Figure 9a-b), whereas there is only a slight difference for the Ideal
362 configuration (Figure 9c-d). Also, the high frequency scenario of the HOYA configuration is
363 relatively less sensitive to low SNR than other scenarios (Figure 9b).
364
365 The explosions analyzed here do not have as much non-isotropic energy as has historically been
366 observed at NTS and in other regions (Walter and Patton, 1990; Ekstrom and Richards, 1994).
367 This may be due to the "wearing out" of the test site over time (Aki and Tsai, 1972), so future
368 work will expand the dataset of explosions to encompass other regions exhibiting exotic records
369 like the "reversed" Rayleigh waves observed for the 1998 Indian tests (Walter and Rodgers,
370 1999).
371
372 6. Conclusions
373
374 Nuclear test explosions from NTS and earthquakes from the surrounding region separate into
375 specific populations according to source-type parameters, which are based on relative
376 magnitudes of isotropic and deviatoric moments. The separation allows for anomalous event
377 identification and discrimination between explosions, earthquakes, and collapses. Synthetic tests
378 show that a mislocation in depth and small deviations in a simple 1D velocity model still recover
379 a significant isotropic component, though Earth complexity is inadequately represented by a
380 three-layer structure. We also assess error due to vanishing traction at the free surface and are
381 able to resolve a reliable mechanism at depths greater than 300 m for data with a good SNR.
382
383 7. Acknowledgements
384

390
391 8. References
392

393 Aki, K. and Y.-B. Tsai (1972). Mechanism of love-wave excitation by explosive sources, J.
394   Geophys. Res., 77(8), 1452-1475.
395 Bowers, D and W. R. Walter, (2002), Discriminating between large mine collapses and
396   explosions using teleseismic P waves, *Pure. Appl. Geophys., 159*, 803-830.
397 Bowers, D. and J.A. Hudson (1999). Defining the scalar moment of a seismic source with a
398   general moment tensor, Bull. Seis. Soc. Amer., 89(5), 1390-1394.
399 Brune, J. N. and P. Pomeroy (1963). Surface wave radiation for underground nuclear explosions
400   and small magnitude earthquakes, J. Geophys. Res. 68, 5005-5028.
401 Dreger, D. S. and D. V. Helmberger (1990), Broadband modeling of local earthquakes, Bulletin
402   of the Seismological Society of America, 80, 1162-1179.
403 Dreger, D. and B. Woods (2002). Regional distance seismic moment tensors of nuclear
404   explosions; seismic source mechanism through moment tensors, Tectonophysics, 356(1-
405   3), 139-156.
406 Ekstrom, G. and P.G. Richards (1994). Empirical measurements of tectonic moment release in
407   nuclear-explosions from teleseismic surface-waves and body waves, Geophys. J. Int.,
408   117(1), 120-140.
409 Foulger, G. R., B. R. Julian, D. P. Hill, A. M. Pitt, P. E. Malin, and E. Shalev (2004), Non-
410   double-couple microearthquakes at Long Valley caldera, California, provide evidence for
411   hydraulic fracturing, J. Volcanol. Geotherm. Res., 132, 45-71.
412 Gilbert, F. (1971), Excitation of the normal modes of the earth by earthquake sources, The
413   Geophysical Journal of the Royal Astronomical Society, 22, 223-226.
414 Given, J. W. and G.R. Mellman (1986). Estimating explosion and tectonic release source
415   parameters of underground nuclear explosions from Rayleigh and Love wave
416   observations, Tech. rep., Sierra Geophysics Report No. SGI-R-86-126, Kirkland, WA.
417 Herrmann, R. B. and K. Hutchensen (1993). Quantification of MLg for small explosion, Tech.
418   rep., Phillips Laboratory Report PL-TR-93-2070.
419 Hudson, J. A., R. G. Pearce, R. G., and R. M. Rogers (1989). Source type plot for inversion of
420   the moment tensor, J. Geophys. Res., 9(B1), 765-774.
421 Ichinose, G. A., J. G. Anderson, K. D. Smith and Y. Zeng (2003). Source parameters of Eastern
422   California and Western Nevada earthquakes from regional moment tensor inversion,
423   Bull. Seis. Soc. Amer., 93(1), 61-84.
424 Julian, B. R., A. D. Miller and G. R. Foulger (1998). Non-double-couple earthquakes; 1. Theory,
425   Rev. Geophysics, 36(4), 525- 549.
426 Kawakatsu, H. (1991), Insignificant isotropic component in the moment tensor of deep
427   earthquakes, Nature (London), 351, 50-53.
428 Knopoff, L. and M. J. Randall (1970). The compensated linear-vector dipole; a possible
429   mechanism for deep earthquakes, J. Geophys. Res., 75(26), 4957-4963.
430 Kuge, K. and T. Lay (1994), Systematic non-double-couple components of earthquake
431   mechanisms; the role of fault zone irregularity, J. Geophys. Res., 99(B8), 15,457-15,467.

432 Langston, C. A. (1981). Source inversion of seismic waveforms; the Koyna, India, earthquakes
433   of 13 September 1967, Bull. Seis. Soc. Amer., 71(1), 1-24.
434 Minson, S. and D. Dreger (2007). Improved seismic moment tensor inversion, Geophys J. Int..
435 Muller, G. (1973). Seismic moment and long-period radiation of underground nuclear
436   explosions, Bull. Seis. Soc. Amer., 63(3), 847-857.
437 Panning, M., D. Dreger and H. Tkalcic (2001). Near-source velocity structure and isotropic
438   moment tensors; a case study of the long valley caldera, Geophys. Res. Lett., 28(9),
439   1815-1818.
440 Pasyanos, M. E., G. A. Franz and A. L. Ramirez (2006). Reconciling a geophysical model to
441   data using a Markov Chain Monte Carlo algorithm: An application to the Yellow Sea-
442   Korean Peninsula region, J. Geophys. Res., 111(B3), B03313.
443 Patton, H. J. (1988). Source models of the Harzer explosion from regional observations of
444   fundamental-mode and higher mode surface waves, Bull. Seis. Soc. Amer., 78(3), 1133-
445   1157.
446 Patton, H. J. (1991). Seismic moment estimation and the scaling of the long-period explosion
447   source spectrum, in Explosion Source Phenomenology, *American Geophysical Union*
448   *Monograph, 65,* edited by Taylor, Patton and Richards.
449 Pechmann, J. C., W. R. Walter, S. J. Nava, and W. J. Arabasz (1995). The February 3, 1995 ML
450   5.1 seismic event in the trona mining district of southwestern Wyoming, *Seism. Res.*
451   *Lett., 66*, 25-34.
452 Press, F. and C. Archambeau (1962). Release of tectonic strain by underground nuclear
453   explosions, *J. Geophys. Res. 67*, 337-343.
454 Riedesel, M. and T. H. Jordan (1989). Display and assessment of seismic moment tensors, Bull.
455   Seis. Soc. Amer., 79(1), 85-100.
456 Saikia, C. K. (1994). Modified frequency-wavenumber algorithm for regional seismograms using
457   Filon's quadrature; modelling of Lg waves in Eastern North America, Geophys. J. Int.,
458   118(1), 142-158.
459 Sileny, J. (2004). Regional moment tensor uncertainty due to mismodeling of the crust,
460   Tectonophysics, 383(3-4), 133-147.
461 Sileny, J. and V. Vavrycuk (2002). Can unbiased source be retrieved from anisotropic
462   waveforms by using an isotropic model of the medium?; Seismic source mechanism
463   through moment tensors, Tectonophysics, 356(1-3), 125-138.
464 Song, X. J., D. V. Helmberger and L. Zhao (1996). Broad-band modelling of regional
465   seismograms; the basin and range crustal structure, Geophys. J. Int., 125(1), 15-29.
466 Springer, D. L., G. A. Pawloski, J. L. Ricca, R. F. Rohrer and D. K. Smith (2002). Seismic
467   source summary for all U.S. below-surface nuclear explosions, Bull. Seis. Soc. Amer.,
468   92(5), 1806-1840.
469 Templeton, D. C. and D. S. Dreger (2006), Non-double-couple earthquakes in the Long Valley
470   volcanic region, Bulletin of the Seismological Society of America, 96, 69-79.
471 Toksoz, M. N. and H. H. Kehrer (1972). Tectonic strain release by underground nuclear
472   explosions and its effect on seismic discrimination, Geophys. J. Roy. Aston. Soc., 31(1-
473   3), 141-161.
474 Vasco, D. W. (1990). Moment-tensor invariants; searching for non-double-couple earthquakes,
475   Bull. Seis. Soc. Amer., 80(2), 354-371.

476   Walter, W. R. (1993). Source parameters of the June 29, 1992 Little Skull Mountain earthquake
477   from complete regional waveforms at a single station, Geophys. Res. Lett., 20(5), 403-
478   406.
479   Walter, W. R. and H. J. Patton (1990). Tectonic release from the soviet joint verification
480   experiment, Geophys. Res. Lett., 17(10), 1517-1520.
481   Walter, W. R., and A. J. Rodgers (1999). Regional waveform modeling in Southwestern Asia;
482   tectonic release from the May 11, 1998 Indian nuclear tests; SSA-99 94th annual
483   meeting; Meeting abstracts, Seismological Research Letters, 70(2), 228.
484   Walter, W. R., K. D. Smith, J. L. O'Boyle, T. F. Hauk, F. Ryall, S. D. Ruppert, S. C. Myers, R.
485   Abbot and D. A. Dodge (2004). An assembled western United States Dataset for regional
486   seismic analysis, LLNL, UCRL-TR-206630.
487   Wessel, P., and W. H. F. Smith (1998). New, improved version of generic mapping tools
488   released, in American Geophysical Union, San Francisco, Vol. 79, 579.
489   Woods, B. B., S. Kedar, and D. V. Helmberger (1993), M (sub L) :M (sub O) as a regional
490   seismic discriminant, Bulletin of the Seismological Society of America, 83, 1167-1183.
491
492

492 Figure 1. Map of the Western US with stations (blue inverted triangles), earthquakes (yellow
493 stars), explosions (red stars), and collapses (green stars) used in this study. The bottom panel is a
494 blow-up of the Nevada Test Site (NTS) region with the NTS outlined in black and in the top
495 panel in red. The top panel also shows the LLNL network (white triangles) and stations used in
496 the explosion analysis (orange triangles). The location of the HOYA test explosion (Figure 3)
497 and Little Skull Mt. earthquake (Figure 2) are also given.

499 Figure 2. Moment tensor analysis of the 1992 Little Skull Mt. earthquake. a) The full moment
500 tensor elements (in 10^{17} N-m) and mechanism (lower hemisphere projection) are shown along
501 with the deviatoric (DEV) and isotropic (ISO) component. The diameter of the mechanism is
502 related to its relative moment, which is given below the mechanism in N-m.
503 b) Data (solid grey) compared with synthetic waveforms (dashed black) produced by the full
504 mechanism shown in (a). The station name with azimuth; distance and maximum displacement
505 (cm) are to the left of the data (solid line) and fit (dashed line) produced by inversion in the 20-
506 50 sec passband.

508 Figure 3. Moment tensor analysis of the 1991 HOYA nuclear test explosion similar to that given
509 in Figure 2 where the moment tensor elements are in 10^{16} N-m. b) Data is bandpassed between
510 20-50 sec except LAC and MNV (LLNL network) which are bandpassed between 10-30 sec and
511 note that BKS is on a different time scale.

513 Figure 4. Source-type plot for the Little Skull Mt. earthquake (dark grey circle), NTS test HOYA
514 (light grey diamond), and bootstrap population of the NTS test DIVIDER (black dots) along with
515 its 95% confidence region (grey ellipse). a) The source-type parameters (k, -2ε) given on a linear
516 plot. b) The source-type plot of Hudson et al. (1989) with theoretical mechanisms plotted as well.

518 Figure 5. Source-type plot of the 12 earthquakes (blue), 17 explosions (red), 3 collapses (green),
519 and their associated 95% confidence regions (shaded) analyzed in this study. The magnitude of
520 the event is given by the symbol. The abscissa measures the amount of volume change for the
521 source and the ordinate measures the departure from pure DC. Theoretical mechanisms (crosses)
522 are plotted for comparison.

524 Figure 6. Sensitivity analysis geometry for the HOYA (black triangle) and Ideal (white inverted
525 triangle) station configuration.

527 Figure 7. Sensitivity analysis. a) Noise is added to the inversion of 20-50 sec synthetic data while
528 velocity model and depth (1 km) are kept fixed for the HOYA (circle) and Ideal (triangle)
529 scenarios. b) The inversion using the HOYA configuration is carried out assuming an incorrect
530 depth while velocity model is kept fixed for data in the 20-50 sec (circle) and 10-50 sec (triangle)
531 band. c) The inversion using the HOYA configuration for 20-50 sec synthetic data is carried out
532 for different three-layer velocity models where the data is not shifted relative to the Green's
533 functions (left panel, circles) and allowed to shift less than 5 sec (right panel, triangles). The
534 symbols are colored as a function of variance reduction (VR).

536 Figure 8. Moment tensor analysis of the 1992 DIVIDER nuclear test explosion similar to that
537 given in Figure 2 where the moment tensor elements are in 10^{13} N-m. b) Data is bandpassed

538   between 10-50 sec except KNB and MNV (LLNL network) which are bandpassed between 10-
539   30 sec and note that MHC and WDC are on a different time scale.
540
541   Figure 9. Vanishing traction sensitivity. Synthetic data for a pure explosion ($k=1$) is inverted at
542   depths less than 1 km for varying SNR and the four scenarios discussed in the text. a-d) Resolved
543   M_{ISO} for SNR values of 2 (circle) 6 (inverted triangle) and 10 (triangle) where the value for an
544   inversion without noise (SNR=∞) is given by the black line (100%). k is given by the color. e-h)
545   Resolved M_{DEV} for SNR values of 2 (circle) 6 (inverted triangle) and 10 (triangle) where the total
546   scalar moment for an inversion without noise (SNR=∞) is given by the black line (100%), and
547   M_{DEV} should be 0. -2ε is given by the color. i-l) Moment tensor elements for data with an
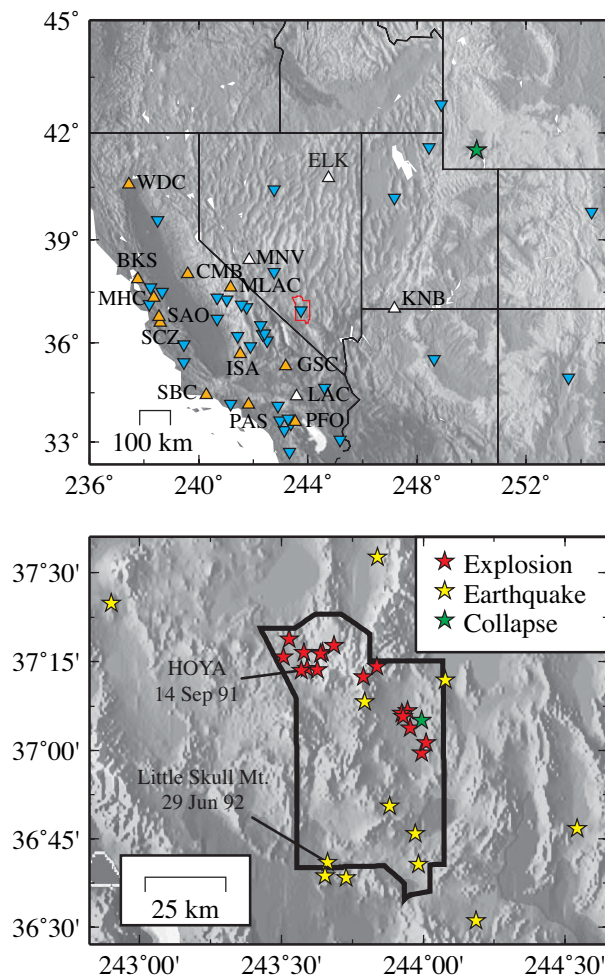548   SNR=10. m-p) Moment tensor elements for data with an SNR=6.

Figure 1
Ford et al., 2008
Version 1

a) Little Skull Mt. Earthquake, 29 Jun 92

$$M = \begin{bmatrix} 0.38 & -1.31 & -0.85 \\ -1.31 & 2.16 & 0.81 \\ -0.85 & 0.81 & -3.46 \end{bmatrix}$$

DEV

ISO

P

T

=

+

$M_0 = 3.7 \times 10^{17}$

$M_0 = 3.4 \times 10^{17}$

$M_0 = 0.3 \times 10^{17}$

b) Waveform fits

CMB
294
404

GSC
201
159

ISA
243
234

KNB
81
302

PAS
214
331

PFO
185
337

SAO
273
472

Tangential

Radial

Vertical
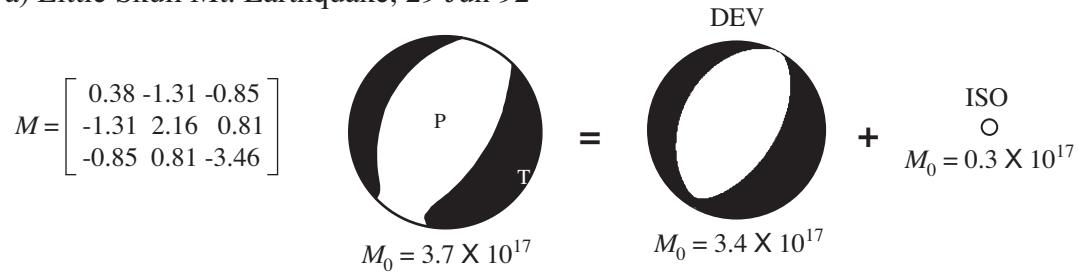
32 s

Figure 2
Ford et al., 2008
Version 1

a) HOYA Explosion, 14 Sep 91

$$M = \begin{bmatrix} 0.90 & -0.30 & 0.12 \\ -0.30 & 1.03 & 0.01 \\ 0.12 & 0.01 & 1.57 \end{bmatrix}$$
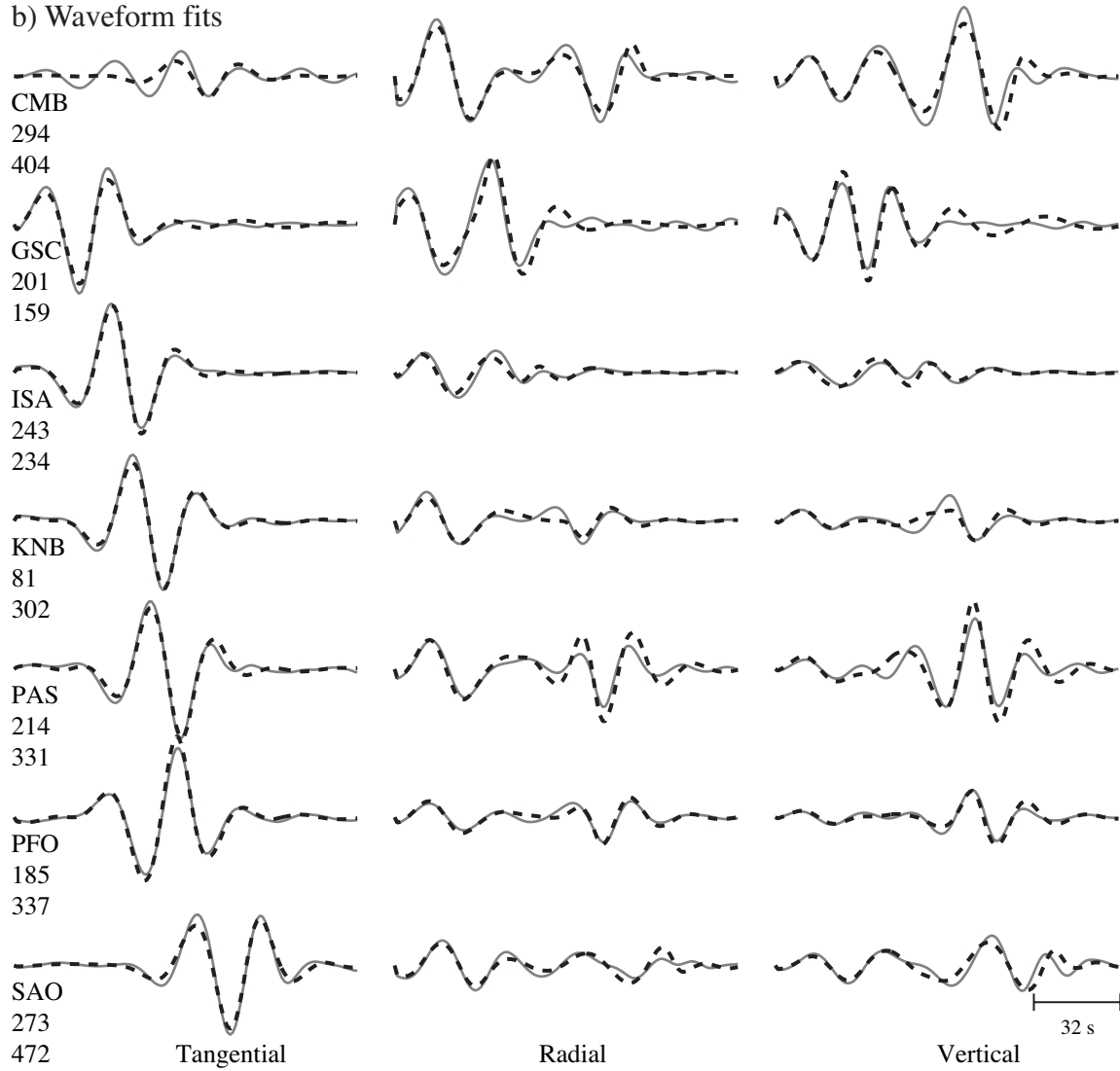
ISO

DEV

=

+

$M_0 = 0.5 \times 10^{16}$

$M_0 = 1.2 \times 10^{16}$

$M_0 = 1.7 \times 10^{16}$

b) Waveform fits

LAC
180
315

32 s

MNV
312
202

GSC
189
216

ISA
227
252

PAS
205
376

PFO
180
401

SBC
225
428

BKS
280
518

48 s

Tangential

Radial

Vertical
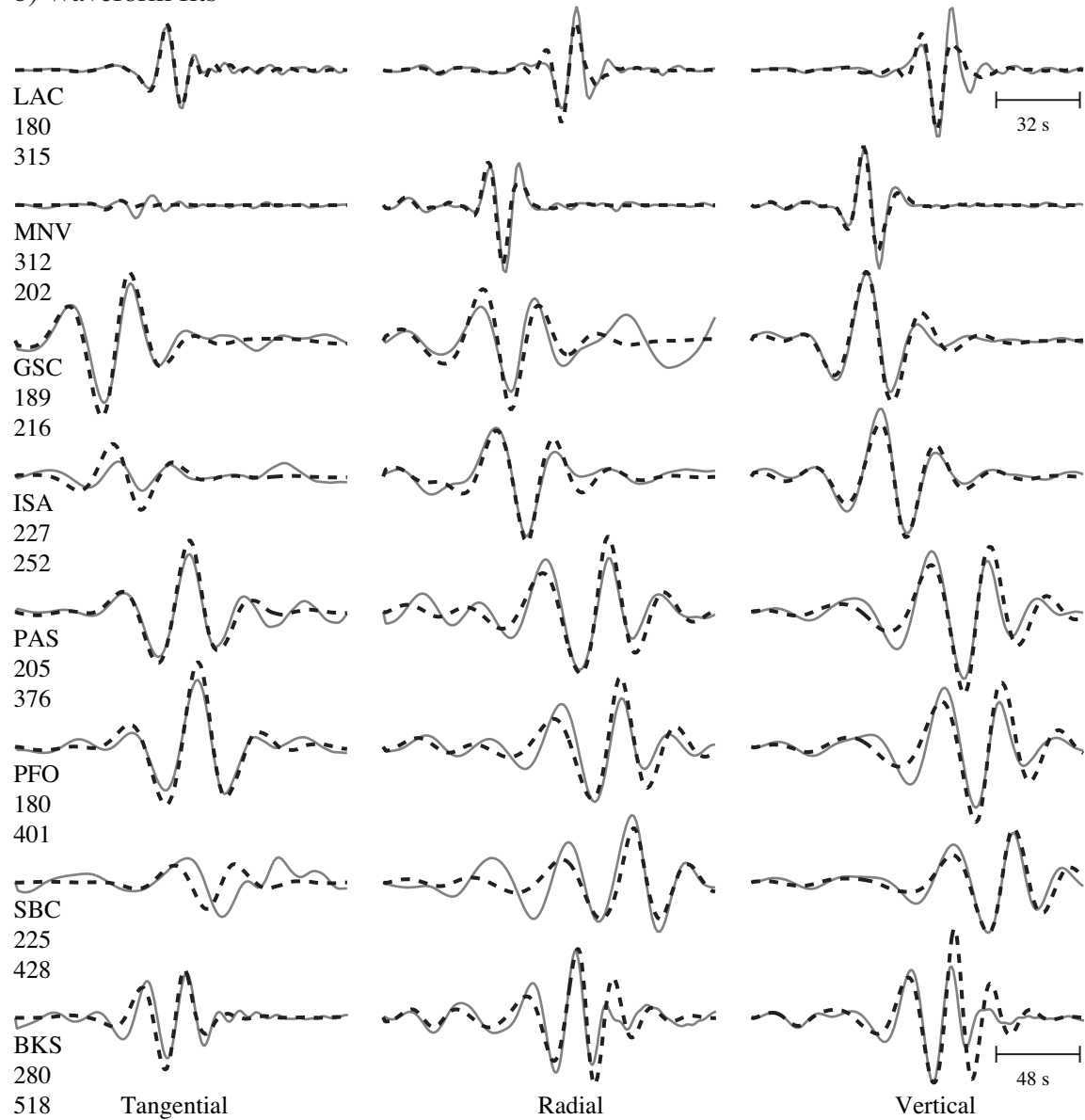
Figure 3
Ford et al., 2008
Version 1

1.0

0.5

k 0.0

-0.5

-1.0

-1.0   -0.5   0.0   0.5   1.0

-2□

Explosion

+CLVD

DC

–CLVD

Implosion

● Little Skull Mt.
   Earthquake

◇ HOYA Explosion

⊙ DIVIDER Explosion
   95% Confidence Ellipse
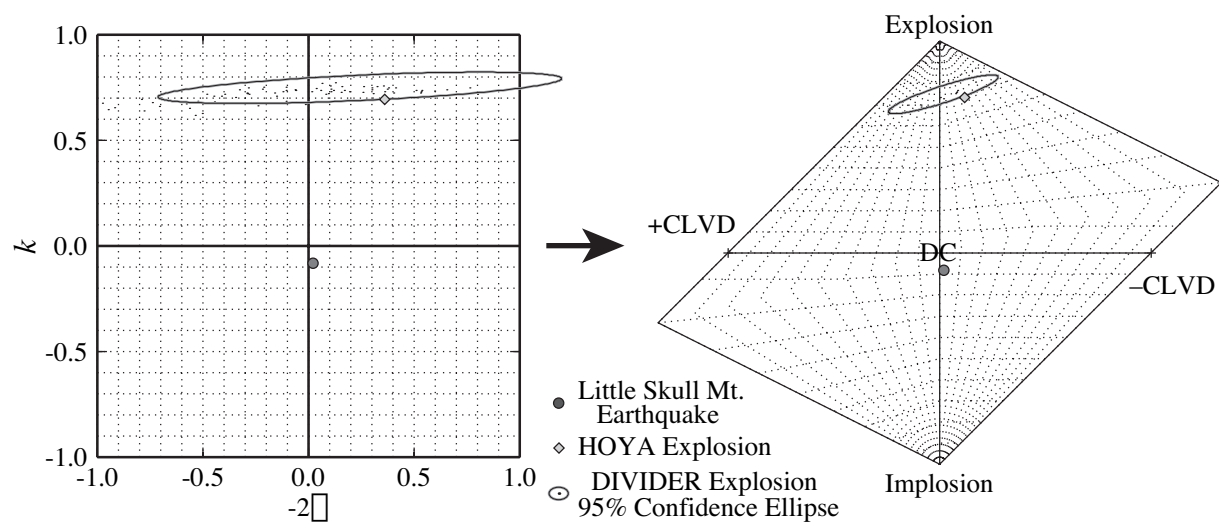
Figure 4
Ford et al., 2008
Version 2

Explosion

+Crack

+Dipole

+CLVD

DC

−CLVD

−Dipole

−Crack

Implosion

■ 5 < M_W < 5.64	⬤ Earthquake
⬤ 4 < M_W < 5	⬤ Explosion
▲ 3.45 < M_W < 4	⬤ Collapse
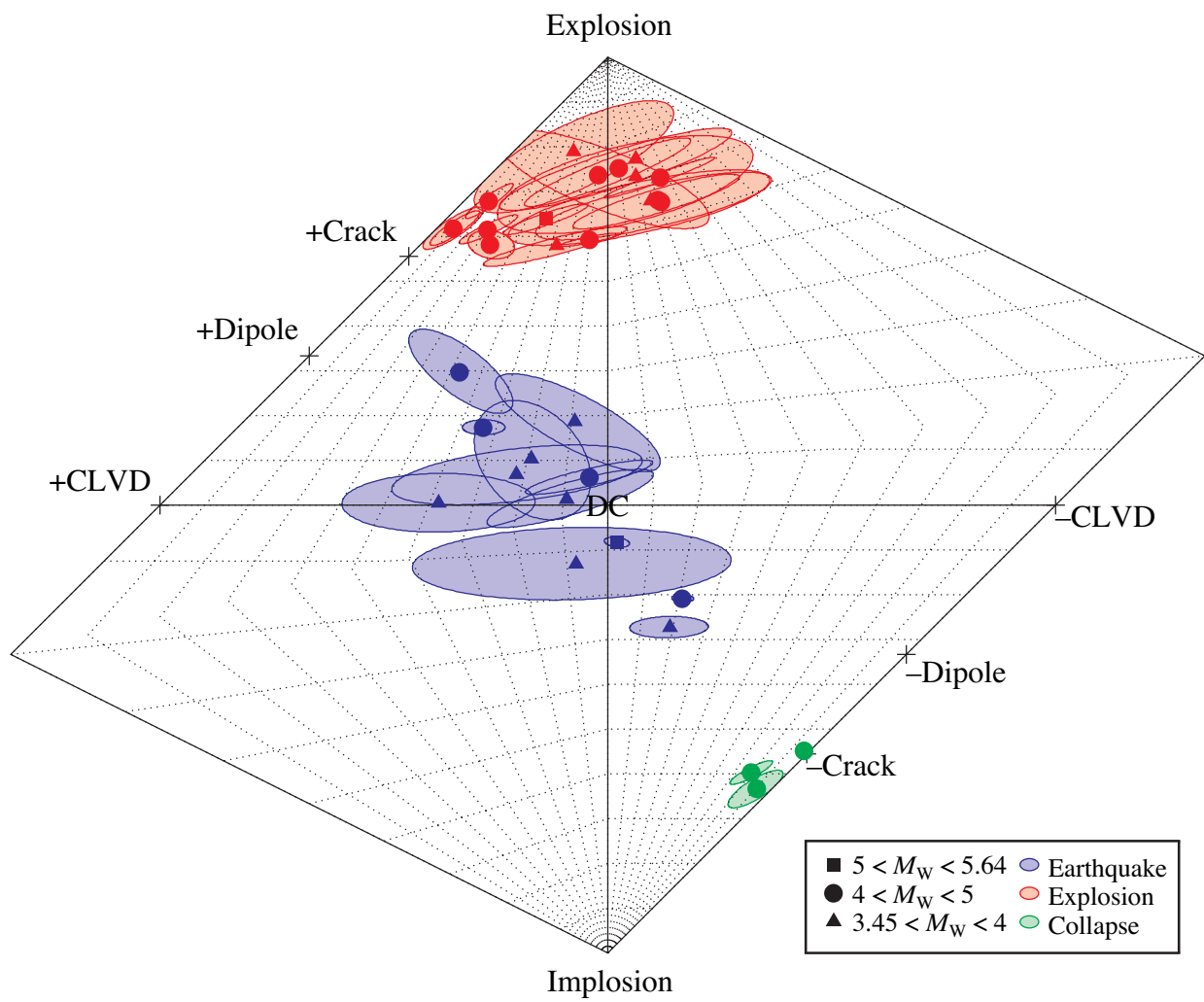
Figure 5
Ford et al., 2008
Version 1

a) Noise (20-50s)
b) Depth (HOYA)
c) Velocity model (HOYA 20-50s)
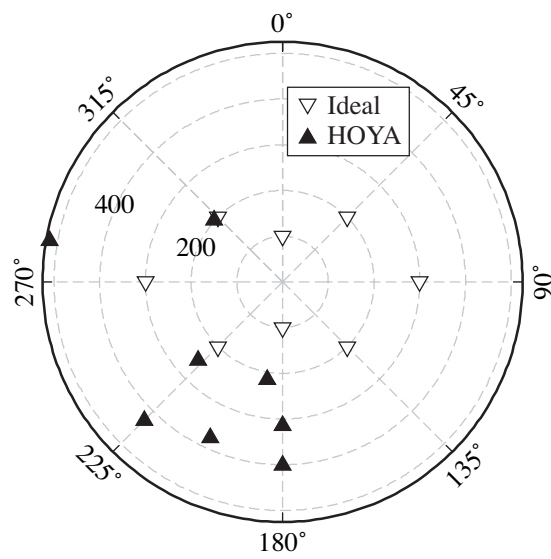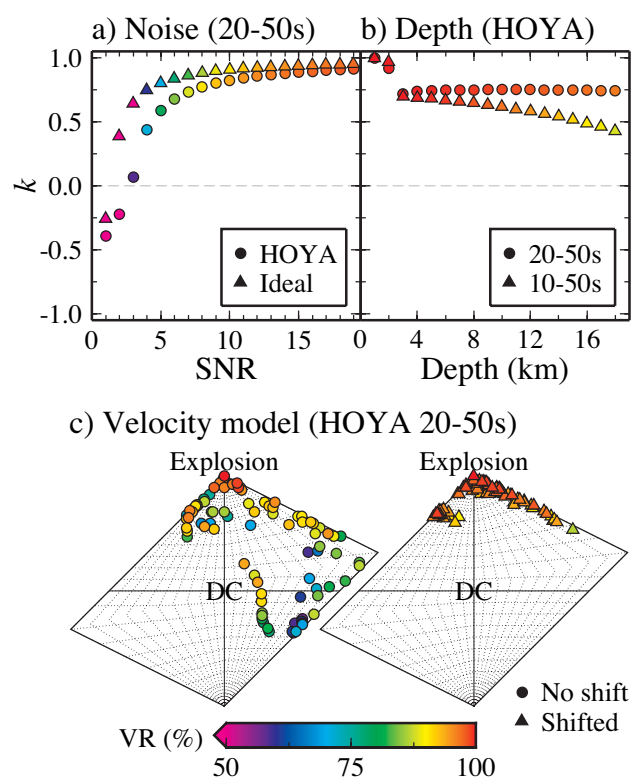
Figure 7
Ford et al., 2008
Version 1

a) DIVIDER Explosion, 23 Sep 92

$$M = \begin{bmatrix} 22.48 & -6.22 & -0.08 \\ -6.22 & 30.31 & 3.99 \\ -0.08 & 3.99 & 31.89 \end{bmatrix}$$

ISO

DEV

=

+

$M_0 = 1.0 \times 10^{14}$

$M_0 = 2.8 \times 10^{14}$

$M_0 = 3.8 \times 10^{14}$

b) Waveform fits

GSC
201
204

ELK
9
418

CMB
287
405

32 s

MHC
276
503

WDC
307
693

48 s

KNB
89
282

MNV
310   Tangential   Radial   Vertical   32 s
247
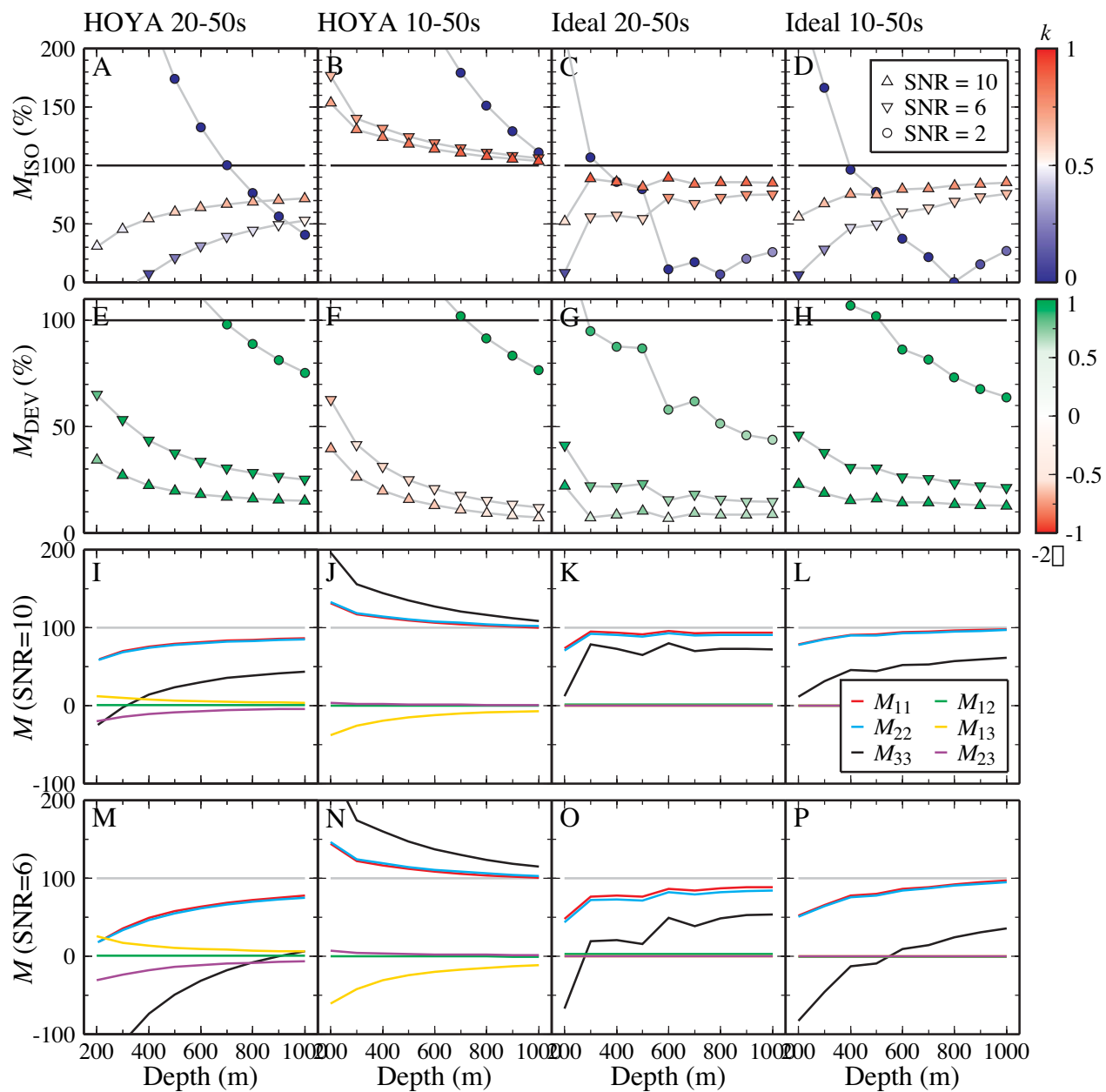
Figure 9
Ford et al., 2008
Version 1

Table 1. Event list[1]

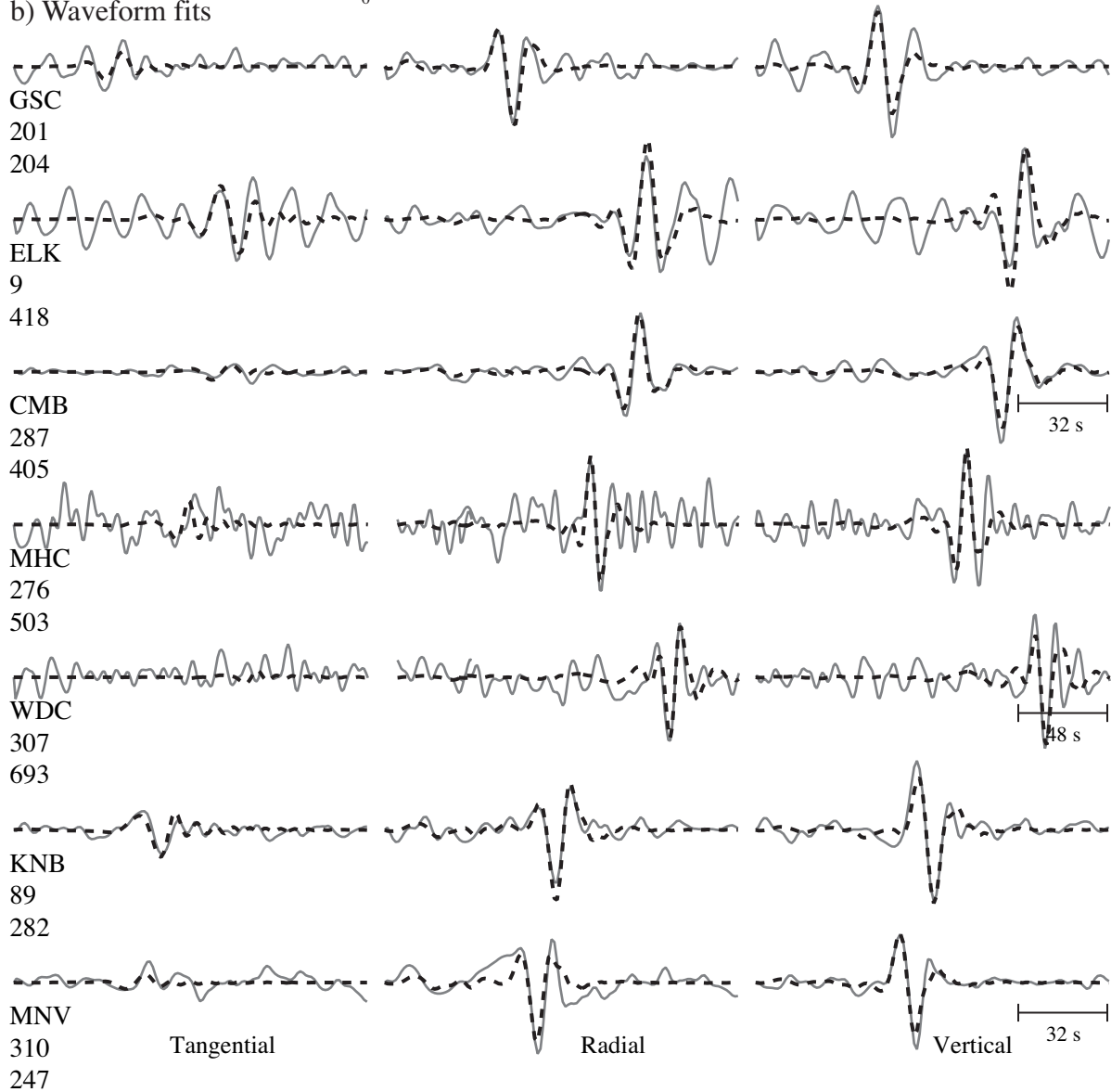| Name[2]	Date[3]	Time[3]	Latitude[3]	Longitude[3]	Depth (m)[4]	Magnitude[6]
KERNVILLE[P]	1988/02/15	18:10:00.09	37.314	-116.472	542	5.30_L^{NCSN}
AMARILLO[P]	1989/06/27	15:30:00.02	37.275	-116.354	640	4.90_L^{NCSN}
DISKO ELM[R]	1989/09/14	15:00:00.10	37.236	-116.164	261	4.40_L^{NCSN}
HORNITOS[P]	1989/10/31	15:30:00.09	37.263	-116.492	564	5.40_L^{NCSN}
BARNWELL[P]	1989/12/08	15:00:00.09	37.231	-116.410	601	5.30_L^{NCSN}
METROPOLIS[Y]	1990/03/10	16:00:00.08	37.112	-116.056	469	4.94_d^{NCSN}
BULLION[P]	1990/06/13	16:00:00.09	37.276	-116.421	674	5.34_d^{NCSN}
AUSTIN[Y]	1990/06/21	18:15:00.00	36.993	-116.005	350	4.11_d^{NCSN}
HOUSTOP[N]	1990/11/14	19:17:00.07	37.227	-116.372	594	4.86_d^{NCSN}
COSO[Y]	1991/03/08	21:02:45.08	37.104	-116.075	417[5]	4.50_L^{NCSN}
BEXAR[P]	1991/04/04	19:00:00.00	37.296	-116.314	629	5.08_d^{NCSN}
HOYA[P]	1991/09/14	19:00:00.08	37.226	-116.429	658	5.40_L^{NCSN}
LUBBOCK[Y]	1991/10/18	19:12:00.00	37.063	-116.046	457	4.75_d^{NCSN}
BRISTOL[Y]	1991/11/26	18:35:00.07	37.096	-116.070	457	4.80_L^{NCSN}
JUNCTION[P]	1992/03/26	16:30:00.00	37.272	-116.361	622	4.82_{Lg}^{NCSN}
HUNTERS TROPHY[R]	1992/09/18	17:00:00.08	37.207	-116.211	385	3.87_d^{NCSN}
DIVIDER[Y]	1992/09/23	15:04:00.00	37.021	-115.989	340	4.13_d^{NCSN}
Little Skull Main	1992/06/29	10:14:21.89	36.6385	-116.2722	4530	5.31_d^{NCSN}
Little Skull Aftershock	1992/07/05	06:54:10.72	36.6767	-116.0178	6590	4.19_d^{NCSN}
Timber Mountain	1995/07/31	12:34:45.03	37.1363	-116.2057	7010	3.58_d^{NCSN}
Amargosa	1996/09/05	08:16:56.09	36.6827	-116.3378	5000	3.38_d^{NCSN}
Groom Pass	1997/04/26	01:49:35.58	37.1987	-115.9220	6040	3.72_d^{NCSN}
Indian Springs	1997/06/14	19:48:19.93	36.5172	-115.8133	7020	3.39_d^{NCSN}
Calico Fan	1997/09/12	13:36:54.20	36.8422	-116.1182	16560	3.70_d^{NCSN}
Warm Springs	1998/12/12	01:41:30.33	37.5437	-116.1605	2870	4.27_d^{NCSN}
Frenchman Flat 1	1999/01/23	03:00:34.82	36.7640	-116.0277	7410	3.45_d^{NCSN}
Frenchman Flat 2	1999/01/27	10:44:17.80	36.7790	-115.4578	8850	4.18_d^{NCSN}
Little Skull	2002/06/14	12:40:45.82	36.6438	-116.3448	8750	4.32_d^{NCSN}
Ralston	2007/01/24	11:30:16.10	37.4133	-117.0986	6090	4.09_d^{UNR}
ATRISCO Hole	1982/08/05	14:21:00	37.0842	-116.0065	640	3.50_S^{LNLL}
Trona Mine 1	1995/02/03	15:26:10.69	41.53	-109.64	1000	5.30_b^{NEIC}
Trona Mine 2	2000/01/30	14:46:51.31	41.46	-109.68	1000	4.40_b^{NEIC}

[1] Names in caps are NTS explosions, last three events are collapses, and all others are earthquakes.
[2] Superscript refers to NTS region where P = Pahute Mesa; R = Rainier Mesa; Y = Yucca
[3] Explosion data from Springer et al. (2002)
[4] Explosion depth of burial from Springer et al. (2002)
[5] This is the average depth of the 3 COSO shots (BRONZE, GRAY, and SILVER)
[6] Subscript refers to magnitude type and superscript refers to magnitude source

Table 2. Velocity model (Song et al., 1996)

Thick (km)	V_α (km/s)	V_β (km/s)	ρ (g/cc)	Q_α	Q_β
2.5	3.6	2.05	2.2	100.0	40.0
32.5	6.1	3.57	2.8	286.0	172.0
∞	7.85	4.53	3.3	600.0	300.0

Table 3. Event parameters ($\times 10^{20}$ dyne-cm)[1]

Name	M_W	M_{11}	M_{12}	M_{13}	M_{22}	M_{23}	M_{33}	k	-2ε
KERNVILLE	4.75	755.6	15.3	-32.6	707.1	83.4	1696.9	0.62	-0.90
AMARILLO	4.16	77.9	-21.4	29.6	156.8	28.2	191.6	0.64	0.31
DISKO ELM	3.53	9.6	-4.4	-2.8	10.2	2.1	24.2	0.58	-0.27
HORNITOS	4.72	835.1	-22.3	79.9	756.3	21.6	1516.1	0.68	-0.83
BARNWELL	4.73	548.1	-264.2	91.4	711.8	210.3	1496.6	0.59	-0.10
METROPOLIS	4.07	118.2	-3.2	0.8	139.8	-29.9	95.9	0.74	-0.08
BULLION	5.05	2043.2	-481.6	172.7	2430.5	574.9	4568.2	0.64	-0.38
AUSTIN	3.60	17.6	-6.2	0.9	15.9	4.8	28.9	0.65	0.26
HOUSTON	4.67	520.0	-72.2	-14.3	555.5	10.1	1269.2	0.62	-0.70
COSO	3.64	18.2	-2.8	5.9	26.9	-0.5	33.4	0.71	0.21
BEXAR	4.62	591.6	-139.8	43.5	792.7	-95.7	994.9	0.74	0.09
HOYA	4.75	898.1	-301.5	118.0	1034.9	9.5	1572.4	0.69	0.36
LUBBOCK	3.99	79.3	-6.3	8.7	90.1	-3.0	119.5	0.79	-0.36
BRISTOL	4.06	56.1	-21.3	19.9	101.5	-3.6	138.3	0.65	0.30
JUNCTION	4.71	592.6	-24.2	-374.2	658.7	30.8	1294.5	0.58	-0.63
HUNTERS TROPHY	3.62	14.6	-0.7	-2.8	14.9	1.8	33.4	0.62	-0.92
DIVIDER	3.65	22.5	-6.2	-0.1	30.3	3.9	31.9	0.75	0.24
Little Skull Main	5.64	3802.5	-13035.1	-8533.9	21603.9	8079.6	-34594.9	-0.08	0.02
Little Skull Aftershock	4.17	36.9	-205.6	7.5	-4.8	-3.3	9.6	0.06	-0.04
Timber Mountain	3.73	9.2	-42.9	4.0	2.6	6.9	-11.1	0.00	-0.38
Amargosa	3.69	-9.4	-2.7	-9.3	8.2	19.2	-34.7	-0.27	0.19
Groom Pass	3.76	16.2	-46.0	7.5	-3.6	-0.9	-1.5	0.07	-0.22
Indian Springs	3.57	-4.6	-24.2	0.1	-1.6	2.0	-4.6	-0.13	-0.08
Calico Fan	3.74	-8.5	-35.0	-10.5	29.6	-9.9	-5.5	0.10	-0.19
Warm Springs	4.27	-19.7	-192.6	66.7	208.8	23.1	-22.6	0.17	-0.34
Frenchman Flat 1	3.74	23.1	-21.3	-10.2	33.8	2.4	-28.3	0.19	-0.09
Frenchman Flat 2	4.65	418.0	-468.8	-154.6	893.7	47.8	-247.8	0.30	-0.47
Little Skull	4.66	50.1	-313.1	-186.6	329.9	327.6	-1145.3	-0.21	0.21
Ralston	3.85	-0.5	-66.7	16.5	13.8	13.9	-10.4	0.01	-0.09
ATRISCO Hole	4.52	-340.5	11.6	7.5	-347.3	60.2	-744.9	-0.63	0.91
Trona Mine 1	4.75	-559.1	5.8	-90.7	-548.9	-47.3	-1689.6	-0.55	0.97
Trona Mine 2	4.15	-85.0	6.7	0.9	-96.3	-6.5	-241.9	-0.60	0.80

[1] Names in caps are NTS explosions, last three events are collapses, and all others are earthquakes.
1 = North; 2 = East; 3 = Down (Aki & Richards cartesian convention).

Table 4. Velocity model perturbations

Parameter	Value
Sediment Thickness (km)	1 2.5* 4
Moho depth1 (km)	31 35* 40
Sediment V_α (km/s)	3.3 3.6* 5
Crustal V_α (km/s)	6.1* 6.202 6.485
Mantle V_α (km/s)	7.6 7.85* 8.15

* Value from Song et al. (1996)

1 The combination of sediment thicknesses and Moho depths results in crustal thicknesses of 27, 28.5, 30, 31, 32.5*, 34, 36, 37.5, and 39 km.